

# Suzaku and XMM-Newton Observations of the Fornax cluster: Temperature and Metallicity Distribution

Hideyoshi MURAKAMI<sup>1</sup>, Madoka KOMIYAMA<sup>1</sup>, Kyoko MATSUSHITA<sup>1</sup>, Ryo NAGINO<sup>1</sup>,  
Takuya SATO<sup>1</sup>, Kosuke SATO<sup>1</sup>, Madoka KAWAHARADA<sup>2</sup>, Kazuhiro NAKAZAWA<sup>3</sup>,  
Takaya OHASHI<sup>4</sup>, and Yoh TAKEI<sup>2</sup>,

<sup>1</sup>*Department of Physics, Tokyo University of Science, 1-3 Kagurazaka, Shinjuku-ku, Tokyo 162-8601*  
*matusita@rs.kagu.tus.ac.jp*

<sup>2</sup>*Institute of Space and Astronautical Science, Japan Aerospace Exploration Agency, 3-1-1 Yoshinodai, Chuo-ku, Sagami-hara,  
Kanagawa 252-5210*

<sup>3</sup>*Department of Physics, The University of Tokyo, 7-3-1 Hongo, Bunkyo-ku, Tokyo 113-0033*

<sup>4</sup>*Department of Physics, Tokyo Metropolitan University, 1-1 Minami-Osawa, Hachioji, Tokyo 192-0397*

(Received 0 0; accepted )

## Abstract

Suzaku observed a central region and five offset regions within  $0.2 r_{180}$  in the Fornax cluster, a nearby poor cluster, and XMM-Newton mapped the cluster with 15 pointings out to  $0.3 r_{180}$ . The distributions of O, Mg, Si, S, and Fe in the intracluster medium (ICM) were studied with Suzaku, and those of Fe and temperature were studied with XMM. The temperature of the ICM gradually decreases with radius from 1.3 keV at  $0.04 r_{180}$  to 1 keV at  $0.2\text{--}0.3 r_{180}$ . If the new solar abundances of Lodders et al. (2003) and a single-temperature plasma model are adopted, O, Mg, Si, S, and Fe show similar abundances: 0.4–0.6 solar within  $0.02\text{--}0.2 r_{180}$ . This Fe abundance is similar to those at  $0.1\text{--}0.2 r_{180}$  in rich clusters and other groups of galaxies. At  $0.2\text{--}0.3 r_{180}$ , the Fe abundance becomes 0.2–0.3 solar. A two-temperature plasma model yields ICM abundances that are higher by a factor of 1.2–1.5, but gives similar abundance ratios among O, Mg, Si, S, and Fe. The northern region has a lower ICM temperature and higher brightness and Fe abundance, whereas the southern region has a higher ICM temperature and lower brightness and Fe abundance. These results indicate that the cD galaxy may have traveled from the north because of recent dynamical evolution. The cumulative oxygen- and iron-mass-to-light ratios (OMLR and IMLR) within  $0.3 r_{180}$  are more than an order of magnitude lower than those of rich clusters and some relaxed groups of galaxies. Past dynamical evolution might have hindered the strong concentration of hot gas in the Fornax cluster’s central region. Scatter in the IMLR and similarity in the element abundances in the ICM of groups and clusters of galaxies indicate early metal synthesis.

**Key words:** galaxies:abundances — clusters of galaxies:intracluster medium — clusters:individual (the Fornax cluster)

## 1. Introduction

Groups and poor clusters of galaxies represent the building blocks of rich clusters and are the best laboratories for the study of their thermal and chemical history, which is governed by baryons. An important clue to the evolution of galaxies is the elemental abundances in the hot X-ray-emitting gas, e.g., the intracluster medium (ICM), in groups and clusters of galaxies. Metals in the ICM have been synthesized by supernovae (SNe) in galaxies. As a result, the ratios of metal mass in the ICM to the total light from galaxies in clusters or groups, i.e., the metal-mass-to-light ratios, are the key parameters in investigating the chemical evolution of the ICM.

Studies of the scaling relations in the clusters of galaxies have revealed strong deviations in the observed relations from the predictions based on self-similar collapse (Ponman et al. 1999; Ponman et al. 2003; Finoguenov et al. 2007; Rasmussen & Ponman 2009; Johnson et al. 2009; Pratt et al. 2010). The gas density profiles in the

central regions of groups and poor clusters are observed to be shallower than those in the self-similar model, and the relative entropy level is correspondingly higher than that in rich clusters. These deviations are considered to be best characterized by the injection of energy (pre-heating) into the gas before the clusters collapse (Kaiser 1991). Based on ROSAT and ASCA data, Ponman et al. (2003) showed that groups and clusters have significant excess entropy at  $r_{500}$ . Voit et al. (2003) have predicted that a smoothing of the gas density due to pre-heating in infalling subhaloes would boost the entropy production at the accretion shock of clusters, and an excess of entropy is generated in the cluster outskirts. This effect due to smooth accretion should be more important for poorer systems. However, Borgani et al. (2005) discussed that this entropy amplification effect can be reduced by cooling. Recently, using XMM data, Pratt et al. (2010) showed that at  $r_{500}$ , the mass dependence of the entropy excess disappeared. Sun et al. (2009) studied the entropy profiles of groups of galaxies observed with Chandra and found that the dif-

ference in the entropy excess at  $r_{500}$  between groups and clusters is not as large as that by Ponman et al. (2003). The stellar and gas mass fractions within  $r_{500}$  depend on the total system mass (Vikhlinin et al. 2006; Arnaud et al. 2007; Sun et al. 2009; Giodini et al. 2009). These studies found that the stellar-to-total-mass ratios within  $r_{500}$  of the groups are much larger than those in the clusters, whereas the gas mass fraction increases with the system mass.

These poorer systems also differ from richer systems in that their iron-mass-to-light ratios (IMLR) are systematically smaller than those in rich clusters (Makishima et al. 2001). The metal distribution in the ICM is a tracer of the history of gas heating, because both metal enrichment and heating timescales determine the metal distribution in the ICM. The Chandra and XMM observations of nearby groups of galaxies with cool cores found that the Fe abundances of the groups declines with the radius and metal-mass-to-light ratios of groups are much smaller than those of the clusters (Rasmussen & Ponman 2007; Finoguenov et al. 2007; Rasmussen & Ponman 2009; Johnson et al. 2011). On the basis of the Chandra data, Rasmussen & Ponman (2009) discussed the effect of feedback and the history of the more extended star formations in less massive systems. With XMM observations, Johnson et al. (2011) found a difference in the abundance profiles of the cool core and non-cool core groups and discussed the effect of mixing driven by active galactic nuclei (AGN) within the central regions.

O and Mg are predominantly synthesized in SN II, whereas Fe and Si are synthesized in both SN Ia and SN II. Therefore, abundance measurements spanning the range of species from O to Fe are required for the unambiguous determination of the formation history of massive stars. XMM-Newton provided a means of constraining the O and Mg abundances of some systems (Matsushita et al. 2003; Tamura et al. 2003; Matsushita et al. 2007b; Simionescu et al. 2009). However, reliable results have been obtained only for the central regions of very bright clusters or groups of galaxies dominated by cD galaxies. The X-ray imaging spectrometer (XIS; Koyama et al. 2007) onboard Suzaku (Mitsuda et al. 2007) offers an improved line spread function because of its very small low-pulse-height tail in the energy range below 1 keV coupled with a very low background. Therefore, especially for regions of low surface brightness or equivalent width, XIS provides better sensitivity to O lines. The instrumental Al line of the MOS detectors on XMM-Newton causes problems in measuring the Mg abundance in somewhat fainter systems.

The oxygen-mass-to-light ratios (OMLRs) as well as the IMLRs of several clusters of galaxies and several groups of galaxies out to  $0.2\text{--}0.3\ r_{180}$  were measured with Suzaku satellite (Matsushita et al. 2007a; Tokoi et al. 2008; Sato et al. 2007; Sato et al. 2008; Sato et al. 2009a; Sato et al. 2009b; Komiyama et al. 2009; Sato et al. 2010). The difference in the OMLRs between groups and clusters is a factor of about 3–6, and tends to be larger than the IMLR difference, which is a factor of 2–3 (Komiyama et

al. 2009).

The Fornax cluster is a nearby poor cluster with an ICM temperature of 1.3–1.5 keV (Scharf et al. 2005). The X-ray emission shows an asymmetric spatial distribution, and the cD galaxy, NGC 1399, is offset from the center (Paolillo et al. 2002; Scharf et al. 2005), which may be related to large-scale dynamical evolution such as infall motions of galaxies into the cluster (Dunn & Jerjen 2006). The Chandra observations suggest that relative motion may occur between NGC 1399 and the ICM, and that the second brightest elliptical galaxy, NGC 1404, is moving supersonically in the ICM (Scharf et al. 2005; Machacek et al. 2005). The Fe and Si abundances of the ICM within  $\sim 50$  kpc of NGC 1399 were measured with XMM-Newton (Buote 2002). The OMLR and IMLR within  $0.13\ r_{180}$  derived from early Suzaku observations of two fields of the Fornax cluster (Matsushita et al. 2007a) are the smallest among those in the groups of galaxies observed with Suzaku.

In this paper, we describe our study of the ICM of the Fornax cluster for regions within  $0.035\text{--}0.2\ r_{180}$  observed with Suzaku and the temperature and Fe abundance out to  $0.3\ r_{180}$  observed with XMM-Newton. In Section 2, we summarize the observations and data preparation. Section 3 describes our analysis of the data, and in Section 4, the temperature and the O, Mg, Si, S, and Fe abundances are determined. We discuss our results in Section 5.

We use the Hubble constant  $H_0 = 70\text{ km s}^{-1}\text{ Mpc}^{-1}$ . The distance to the Fornax cluster is  $D_L = 19.8\text{ Mpc}$  and  $1'$  corresponds to  $5.70\text{ kpc}$ . The virial radius,  $r_{180} = 1.95\ h_{100}^{-1} \sqrt{k\langle T \rangle / 10\text{ keV}}\text{ Mpc}$  (Markevitch et al. 1998; Evrard et al. 1996), is about 1 Mpc for the average temperature  $k\langle T \rangle = 1.3\text{ keV}$ . In this paper, we use the new abundance table from Lodders et al. (2003). The O and Fe abundances are about 1.7 times and 1.6 times higher than those of Anders & Grevesse (1989), respectively. Unless otherwise specified, errors are quoted at 90% confidence for the single parameter of interest.

## 2. Observations

### 2.1. Suzaku observations

Suzaku performed six pointing observations of the Fornax cluster, as summarized in Table 1. The first observation (hereafter, Center field) was carried out on 2005 September with the pointing direction  $2'$  south and  $1'$  east of NGC 1399. The second one (hereafter, North field) was centered  $13'$  north and  $4'$  east of NGC 1399, and was carried out on 2006 January. Four additional observations were centered  $\sim 30'$  north (hereafter, Far North field), and  $\sim 17'\text{--}27'$  south, northwest, and northeast (hereafter, South, North West, and North East fields, respectively) of NGC 1399. The left panel of Figure 1 shows a  $0.5\text{--}4.0\text{ keV}$  image obtained with these Suzaku observations. The observed region covers a distance of about about  $42'$ , or  $\sim 240\text{ kpc}$  toward the north from NGC 1399: this distance corresponds to  $0.24\ r_{180}$ . To constrain emissions from our Galaxy, we also observed two fields offset of  $\sim 5$  degrees

from NGC 1399 (hereafter, Galactic1 and Galactic2 fields) in 2007 June. The observation log is also shown in Table 1.

The XIS was operated in the nominal mode during these observations. We included the data formats of both  $5 \times 5$  and  $3 \times 3$  editing modes in our analysis using XSELECT (Ver. 2.4a). The analysis was performed using HEASOFT (Ver. 6.6.3) and XSPEC (Ver. 11.3.2ag). After the standard data selection criteria are applied, the exposure times of the four offset fields are 35–56 ks. Those of the Galactic1 and Galactic2 fields are  $\sim 20$  ks.

The spectra of the Center and North fields were accumulated within concentric rings,  $6'–13'$  and  $13'–26'$ , centered on NGC 1399. The spectra of the Far North, South, North West and North East fields were accumulated over the field of view of XIS. Each spectrum was binned to observe details in metal lines, and each spectral bin contained 50 or more counts.

The response of the X-ray telescope (XRT) and XIS for each spectrum was calculated using the `xisrmfgen` response matrix file (RMF) generator, version 2009-02-18. The ancillary response files (ARF) were calculated using `xissimarfgen` (Ishisaki et al. 2007), version 2009-01-08, assuming flat emission, because the Fornax cluster is much more extended than the field of view of the XIS, and ARFs assuming flat-sky emission, a  $\beta$ -model profile, and a point-source are almost the same within the energy range of 0.4 to 5 keV, except for normalization. Slight degradation of the energy resolution was considered in the RMF, and decrease in the low-energy transmission of the XIS optical blocking filter (OBF) was included in the ARF.

The non-X-ray background (NXB) was subtracted from the spectra using a database of night Earth observations (Tawa et al. 2008). We used the spectra within an energy range of 0.4–5.0 keV, because above 5.0 keV, background components dominate the X-ray emission.

## 2.2. XMM-Newton observations

We analyzed 15 pointing XMM-Newton observations of the Fornax cluster (Table 1).

The middle and right panels of Figure 1 show a 0.8–1.2 keV MOS image. The NXB and Cosmic X-ray background (CXB) were not subtracted because this energy band is dominated by the ICM emission. The observed region covers out to  $0.3 r_{180}$  in the east, north and southwest directions. We used the PN, MOS1, and MOS2 detectors and selected events with patterns smaller than 5 and 13 for the PN and MOS, respectively. To screen background flares, we constructed count rate histograms of PN and MOS. Then, we fitted each histogram with a Gaussian and selected the time within  $2.5 \sigma$  of the mean for each histogram. The total exposures after background flares are summarized in Table 1. Because the observations of fields G and L were completely dominated by very high background flares, no exposure time remained.

Spectra were accumulated in pie regions of north, east, south, and west, centered on NGC 1399 as summarized in Figure 1. We also accumulated spectra in the square

**Table 2.** The results of the spectral fitting of the Galactic emission with Suzaku.

Region	$kT_1$ (keV)	$kT_2$ (keV)	Ratio of Norm*	$\chi^2/\text{d.o.f.}$ -
Galactic1	$0.11^{+0.02}_{-0.02}$	$0.37^{+0.09}_{-0.07}$	$0.11^{+0.09}_{-0.06}$	151/129
Galactic2	$0.09^{+0.02}_{-0.02}$	$0.28^{+0.05}_{-0.04}$	$0.10^{+0.15}_{-0.06}$	140/113

\* The ratio of normalizations of higher and lower temperature components.

regions of  $0.1 r_{180} \times 0.1 r_{180}$  ( $17.5' \times 17.5'$ ). Each square region surrounding NGC 1399 is divided into two: one is a small square region  $0.05 r_{180} \times 0.05 r_{180}$  and the other, as shown in Figure 1. When accumulating spectra, luminous point sources and NGC 1404 were excluded. Although we have not screened hot chips of MOS (Kuntz & Snowden 2008), we have verified that exclusions of the hot chips do not affect any results. RMF and ARF corresponding to each spectrum were calculated using SAS v8.0.0. The spectral analysis also used the XSPEC\_v11.3.2ag package.

## 3. Spectral Analysis

### 3.1. Galactic fields observed with Suzaku

To estimate the Galactic emission, we first analyzed the two Galactic fields observed with Suzaku. The Galactic emission, which includes the local hot bubble, the Milky Way halo, and solar wind charge exchange, is empirically fitted with a two-temperature plasma model with redshift  $= 0$  (Lumb et al. 2002; Yoshino et al. 2009). Therefore, we used the two-temperature APEC thermal model for the Galactic emission, with a power-law model for the CXB, and fitted the observed spectra from the Galactic1 and Galactic2 fields. The temperature and normalization of the two components in the Galactic emission were left free, with the metal abundance fixed to the solar level. CXB was modeled by a power-law spectrum with a photon index  $\Gamma = 1.4$ . The normalization of the power-law was allowed to be free. The model spectra, except for the lower-temperature APEC component, were subjected to a common interstellar absorption  $N_H$ , fixed at the Galactic value in the direction of each field by Dickey & Lockman (1990).

The results of the spectral fits are shown in Table 2. Except for the instrumental Al line at 1.5 keV, this model reproduced the spectra well. The derived temperatures of the two APEC components and the ratio of the normalizations of the two Galactic fields are consistent with each other. The derived temperatures,  $\sim 0.1$  keV and  $\sim 0.3$  keV, are consistent with the typical values for the Galactic emission.

### 3.2. The Fornax cluster observed with Suzaku

We first assumed an ICM in each region consisting of a single-temperature vAPEC (Smith et al. 2001) model (hereafter, the 1T model). We fitted all the XIS spectra of each region with the 1T model for the ICM, a power-law model for the CXB, and the two-temperature APEC model for the Galactic components. The temperature,

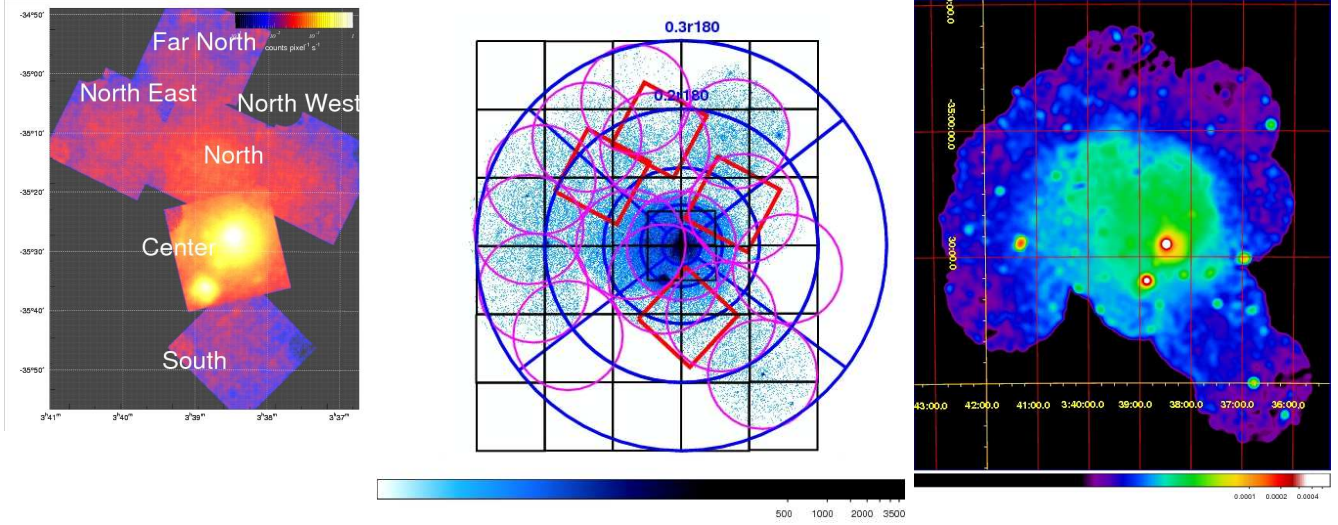


**Fig. 1.** (left) Suzaku-XIS (0.5–4.0 keV) image of the Fornax cluster. The NXB was subtracted and the difference in exposure times was corrected. The Cosmic X-ray background (CXB) was not subtracted. (middle) Raw XMM-MOS image (0.8–1.2 keV) of the Fornax cluster. Magenta circles correspond to field of view of the XMM observations. Red squares indicate the four offset observations with Suzaku. Blue pie and black square regions summarize the accumulation area of spectral analysis. (right) Exposure- and vignetting-corrected and adaptively smoothed XMM-MOS image (0.8–1.2 keV). The NXB and CXB were not subtracted.

**Table 1.** Suzaku and XMM observations of the Fornax cluster and background fields

Fields	Seq. No.	(R.A., Dec.) in J2000.0	Date of obs.	Exp. time (after screenings)
Suzaku observations of the Fornax cluster				
Center	100020010	(3 <sup>h</sup> 38 <sup>m</sup> 35 <sup>s</sup> .7, −35°28′14″.5)	2005/09/13	76 ks
North	800002010	(3 <sup>h</sup> 38 <sup>m</sup> 51 <sup>s</sup> .9, −35°14′23″.6)	2006/01/05	78 ks
Far North	802021010	(3 <sup>h</sup> 38 <sup>m</sup> 55 <sup>s</sup> .9, −34°57′32″.4)	2008/01/14	56 ks
South	803006010	(3 <sup>h</sup> 38 <sup>m</sup> 19 <sup>s</sup> .6, −35°45′49″.1)	2008/07/15	35 ks
North West	803007010	(3 <sup>h</sup> 37 <sup>m</sup> 25 <sup>s</sup> .7, −35°16′52″.7)	2008/07/16	41 ks
North East	803008010	(3 <sup>h</sup> 40 <sup>m</sup> 07 <sup>s</sup> .5, −35°09′04″.1)	2008/07/17	41 ks
Suzaku observations of the Fornax Galactic field				
Galactic1	802037010	(3 <sup>h</sup> 13 <sup>m</sup> 11 <sup>s</sup> .0, −37°40′48″.0)	2007/06/28	20 ks
Galactic2	802040010	(3 <sup>h</sup> 19 <sup>m</sup> 57 <sup>s</sup> .7, −32°04′18″.8)	2007/06/29	21 ks
XMM observations of the Fornax cluster				MOS1, MOS2, PN
A	0550930101	(3 <sup>h</sup> 39 <sup>m</sup> 02 <sup>s</sup> .4, −35°01′55″.2)	2008/06/28	10.6, 11.2, 7.0 ks
B	0550930201	(3 <sup>h</sup> 39 <sup>m</sup> 26 <sup>s</sup> .2, −34°49′37″.2)	2008/06/27	7.6, 6.7, 3.5 ks
C	0550930301	(3 <sup>h</sup> 40 <sup>m</sup> 27 <sup>s</sup> .1, −34°59′16″.8)	2008/07/17	11.4, 11.6, 8.0 ks
D	0550930401	(3 <sup>h</sup> 41 <sup>m</sup> 25 <sup>s</sup> .0, −35°10′04″.8)	2009/02/09	14.5, 15.1, 11.7 ks
E	0550930501	(3 <sup>h</sup> 41 <sup>m</sup> 40 <sup>s</sup> .8, −35°22′51″.6)	2009/02/23	18.1, 17.8, 14.6 ks
F	0550930601	(3 <sup>h</sup> 41 <sup>m</sup> 35 <sup>s</sup> .0, −35°37′48″.0)	2009/02/24	17.7, 17.9, 13.7 ks
G	0550930701	(3 <sup>h</sup> 40 <sup>m</sup> 52 <sup>s</sup> .1, −35°50′02″.4)	2009/02/24	0, 0, 0 ks
J	0550931001	(3 <sup>h</sup> 37 <sup>m</sup> 38 <sup>s</sup> .9, −35°45′18″.0)	2008/06/25	19.1, 19.4, 11.7 ks
L	0550931201	(3 <sup>h</sup> 36 <sup>m</sup> 15 <sup>s</sup> .6, −35°32′56″.4)	2008/06/25	0, 0, 0 ks
N	0550931401	(3 <sup>h</sup> 37 <sup>m</sup> 11 <sup>s</sup> .5, −35°17′34″.8)	2008/06/26	11.0, 11.4, 8.0 ks
NGC 1399	0400620101	(3 <sup>h</sup> 38 <sup>m</sup> 29 <sup>s</sup> .1, −35°27′03″.0)	2006/08/23	99.6, 102.7, 53.2 ks
NGC 1404	0304940101	(3 <sup>h</sup> 38 <sup>m</sup> 51 <sup>s</sup> .9, −35°35′39″.8)	2005/07/30	24.6, 15.0, 17.0 ks
LP 944-20	0055140101	(3 <sup>h</sup> 39 <sup>m</sup> 34 <sup>s</sup> .60, −35°25′51″.0)	2001/01/07	43.0, 43.2, 36.5 ks
RXJ 0337-3457	0210480101	(3 <sup>h</sup> 37 <sup>m</sup> 24 <sup>s</sup> .70, −34°57′29″.0)	2005/01/04	44.3, 44.4, 37.9 ks
NGC 1386	0140950201	(3 <sup>h</sup> 36 <sup>m</sup> 45 <sup>s</sup> .4, −35°59′57″.0)	2002/12/29	15.9, 15.9, 12.8 ks

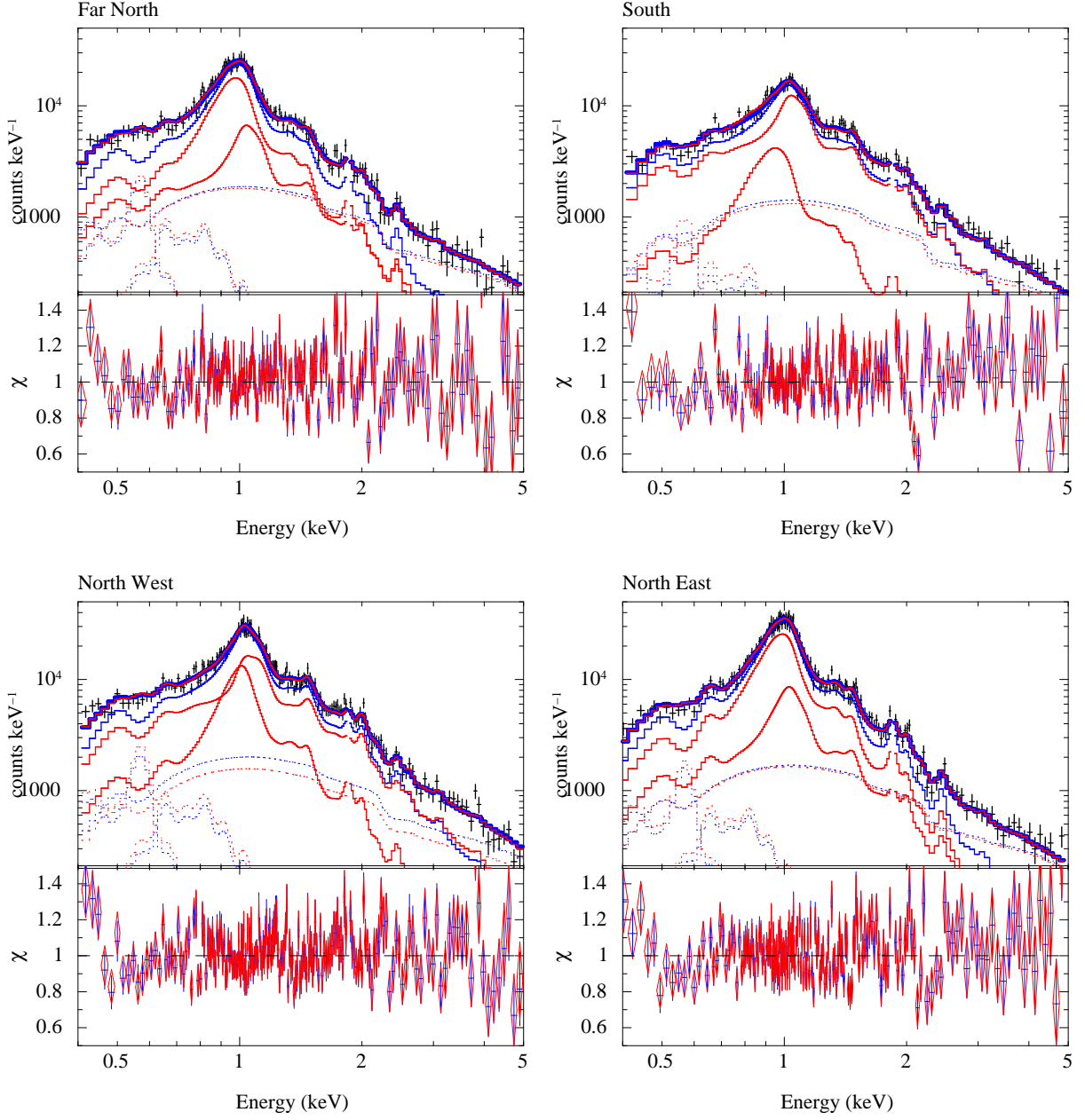


**Fig. 2.** Spectra of the four offset fields from the XIS-1 instruments fitted with the 1T (blue) or 2T (red) model for the ICM (solid lines) and background components (dashed lines) including the power-law and the Galactic components. Lower panels show the data-to-model ratios for the 1T (blue crosses) and the 2T (red diamonds) model fits.

abundances, and normalization of the ICM component of each field were allowed to vary. Here, the metal abundances of He, C, and N were fixed to the solar values. We divided the other metals into six groups: O; Ne; Mg and Al; Si; S, Ar, and Ca; Fe and Ni. The spectral components except for the lower-temperature Galactic emission were subjected to a common interstellar absorption,  $N_{\text{H}}$ , which was allowed to vary for each instrument, considering the systematic uncertainties of contaminants on the XIS detectors. The temperatures of the two Galactic components were fixed at 0.1 keV and 0.3 keV, respectively, and the ratio of the normalizations of the higher- and lower-temperature components was fixed at 0.1, which was the best-fit value for the two Galactic fields.

The results are shown in Table 3 and the fitted spectra of the four new offset fields are shown in Figure 2. The derived reduced  $\chi^2$  values were  $\sim 1$ , and the spectra of the Fornax cluster were consistently reproduced by the sum of the ICM model and this Galactic component.

We also applied a two-temperature model for the ICM (hereafter, the 2T model), where the abundances of each metal in the two components were assumed to have the same value. The results are shown in Table 3 and Figure 2. Compared to the 1T model, the reduced  $\chi^2$  decreased slightly by several percent, whereas, the metal abundances increased by several tens of percent. As shown in Table 3, F-test probabilities support an addition of the second temperature component in most of the systems. However, considering the possible systematic uncertainties in the Fe-L and background components, we cannot determine whether the 2T model is better than the 1T model because the 1T model still represents the spectra fairly well.

To study the systematic uncertainties in the modeling of the Galactic components, we fitted the spectra with the 1T or 2T model for the ICM in a similar manner, except that the normalizations of the two Galactic components of each field were allowed to be free. The temperature and abundances of Ne, Mg, Si, S, and Fe, and the weighted averages of O/Fe, Ne/Fe, Mg/Fe, Si/Fe, and S/Fe were almost the same within 10–20%, although the best-fit values of the O abundances were changed by 0.1–0.2 solar.

### 3.3. XMM analysis

We used the spectra from MOS1, MOS2 and PN in the energy ranges of 0.4–4.0 keV, but ignored the energy range of 1.4–1.6 keV. The spectra in each region (pie and square) were fitted simultaneously with the 1T model for the ICM, the Galactic emission, CXB, and NXB components. Here, the temperatures and normalizations of the Galactic components were fixed at the best-fit values derived from the spectral fitting of the Suzaku data. The abundance ratios were also fixed at the weighted averages of the four offset fields observed with Suzaku (Section 4.3). We modeled the NXB spectrum with a powerlaw/b model and two Gaussians for the instrumental lines at 1.48 keV (Al) and 1.74 keV (Si). The powerlaw/b model is not folded through the ARF, and differs from a power-law. We added two Gaussians at 0.56 keV and 0.65 keV for the solar wind charge exchange. Figure 3 shows represen-

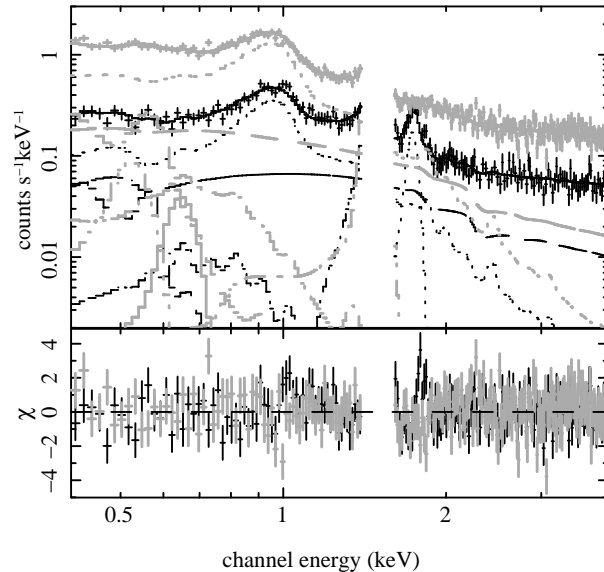


**Fig. 3.** Representative spectra of a square region of MOS1 (black) and PN (gray), fitted with the 1T ICM model. Dotted and other lines corresponds to the ICM components and background, respectively.

tative spectra fitted in this manner. We also fitted the spectra of deep fields in the same energy range and confirmed that this background model reproduced the data well. Most of the spectra were fitted with the 1T model for the ICM with reduced  $\chi^2 \sim 1$ . We also applied the 2T model for the ICM. Within  $0.05 r_{180}$ , the 2T model showed a significantly decreased  $\chi^2$ . We adopted the Fe abundance from the 2T model fits within  $0.05 r_{180}$ .

## 4. Results

### 4.1. Temperature distribution of the ICM

Figure 4 summarizes the temperatures of the  $> 6'$  regions of Suzaku and the pie regions of XMM versus radius of NGC 1399, in comparison with those from the central  $6'$  of NGC 1399 by Matsushita et al. (2007a). The temperatures derived from XMM and Suzaku are mostly consistent with each other.

The observed ICM temperatures are  $\sim 1.2$ – $1.3$  keV at  $0.03$ – $0.1 r_{180}$  which further decreases with radius to  $\sim 1$  keV at  $0.2$ – $0.3 r_{180}$ . The azimuthal dependence of the temperature is largest at  $0.1$ – $0.2 r_{180}$ : the ICM temperatures in the western and southern regions are  $1.2$ – $1.3$  keV and those in the northern and eastern regions are  $\sim 1$  keV. From the 2T model for the ICM, the temperatures of the two components are  $0.8$ – $1$  keV and  $1.3$ – $1.5$  keV (Table 3).

To study the temperature structure in more detail, the ICM temperature map derived from the square regions in the XMM observations is shown in the Figure 5. Here, we did not plot the temperatures of four small square regions around the cD galaxy because we need two temperatures to fit the spectra. At a given distance from NGC 1399, the southwestern regions show higher ICM temperatures than

**Table 3.** The ICM temperature,  $\chi^2$ , and elemental abundances derived from the spectral fits of Suzaku for the Fornax cluster.

Field	$r$ (arcmin)	model	$kT$ (keV)	$kT$ (keV)	$\chi^2/\text{d.o.f.}$	F-test probability*		
Center	6–13	1T	$1.32^{+0.01}_{-0.01}$		1065/934			
Center	6–13	2T	$0.81^{+0.03}_{-0.04}$	$1.50^{+0.05}_{-0.06}$	979.4/933	$1 \times 10^{-18}$		
North	6–13	1T	$1.27^{+0.01}_{-0.01}$		754.4/734			
North	6–13	2T	$0.84^{+0.22}_{-0.19}$	$1.32^{+0.23}_{-0.05}$	731.3/732	$1 \times 10^{-5}$		
North	13–26	1T	$1.16^{+0.01}_{-0.01}$		1058/956			
North	13–26	2T	$1.02^{+0.03}_{-0.11}$	$1.45^{+0.16}_{-0.24}$	975.4/954	$1 \times 10^{-17}$		
North West	7–28	1T	$1.33^{+0.01}_{-0.01}$		521.1/428			
North West	7–28	2T	$1.09^{+0.16}_{-0.08}$	$1.72^{+0.19}_{-0.16}$	504.0/427	0.0002		
South	10–31	1T	$1.27^{+0.02}_{-0.02}$		325.7/275			
South	10–31	2T	$0.84^{+0.15}_{-0.05}$	$1.48^{+0.17}_{-0.14}$	307.0/274	$6 \times 10^{-5}$		
North East	17–36	1T	$1.04^{+0.01}_{-0.01}$		403.1/384			
North East	17–36	2T	$1.00^{+0.04}_{-0.13}$	$1.29^{+1.08}_{-0.77}$	395.3/383	0.006		
Far North	20–42	1T	$1.05^{+0.01}_{-0.01}$		382.6/340			
Far North	20–42	2T	$0.98^{+0.05}_{-0.13}$	$1.43^{+0.72}_{-0.22}$	365.9/339	0.0001		
Field	$r$ (arcmin)	model	O (solar)	Ne (solar)	Mg (solar)	Si (solar)	S (solar)	Fe (solar)
Center	6–13	1T	$0.30^{+0.07}_{-0.07}$	$0.10^{+0.14}_{-0.10}$	$0.25^{+0.06}_{-0.06}$	$0.33^{+0.04}_{-0.04}$	$0.38^{+0.05}_{-0.05}$	$0.38^{+0.02}_{-0.02}$
Center	6–13	2T	$0.41^{+0.09}_{-0.09}$	$0.75^{+0.25}_{-0.23}$	$0.45^{+0.09}_{-0.09}$	$0.46^{+0.06}_{-0.06}$	$0.47^{+0.07}_{-0.07}$	$0.54^{+0.05}_{-0.05}$
North	6–13	1T	$0.44^{+0.12}_{-0.11}$	$0.31^{+0.19}_{-0.19}$	$0.34^{+0.07}_{-0.07}$	$0.45^{+0.05}_{-0.05}$	$0.52^{+0.07}_{-0.07}$	$0.53^{+0.03}_{-0.03}$
North	6–13	2T	$0.54^{+0.14}_{-0.13}$	$0.78^{+0.37}_{-0.29}$	$0.47^{+0.11}_{-0.10}$	$0.53^{+0.07}_{-0.06}$	$0.59^{+0.08}_{-0.08}$	$0.64^{+0.07}_{-0.05}$
North	13–26	1T	$0.43^{+0.10}_{-0.09}$	$0.13^{+0.16}_{-0.13}$	$0.38^{+0.06}_{-0.06}$	$0.36^{+0.04}_{-0.04}$	$0.50^{+0.06}_{-0.06}$	$0.53^{+0.03}_{-0.03}$
North	13–26	2T	$0.63^{+0.14}_{-0.12}$	$0.93^{+0.30}_{-0.27}$	$0.61^{+0.12}_{-0.10}$	$0.51^{+0.07}_{-0.06}$	$0.62^{+0.08}_{-0.08}$	$0.71^{+0.08}_{-0.06}$
North West	7–28	1T	$0.18^{+0.18}_{-0.17}$	$0.55^{+0.30}_{-0.29}$	$0.45^{+0.12}_{-0.11}$	$0.40^{+0.07}_{-0.07}$	$0.37^{+0.09}_{-0.09}$	$0.49^{+0.04}_{-0.04}$
North West	7–28	2T	$0.33^{+0.25}_{-0.22}$	$1.35^{+0.64}_{-0.49}$	$0.70^{+0.21}_{-0.17}$	$0.52^{+0.11}_{-0.09}$	$0.44^{+0.13}_{-0.11}$	$0.72^{+0.11}_{-0.10}$
South	10–31	1T	$0.16^{+0.19}_{-0.16}$	$0.00^{+0.18}_{-0.00}$	$0.19^{+0.11}_{-0.11}$	$0.23^{+0.07}_{-0.07}$	$0.36^{+0.11}_{-0.12}$	$0.34^{+0.04}_{-0.04}$
South	10–31	2T	$0.28^{+0.27}_{-0.23}$	$0.53^{+0.62}_{-0.49}$	$0.40^{+0.22}_{-0.18}$	$0.33^{+0.13}_{-0.11}$	$0.45^{+0.16}_{-0.15}$	$0.50^{+0.13}_{-0.11}$
North East	17–36	1T	$0.40^{+0.17}_{-0.15}$	$0.25^{+0.29}_{-0.25}$	$0.42^{+0.11}_{-0.10}$	$0.35^{+0.07}_{-0.07}$	$0.43^{+0.12}_{-0.11}$	$0.52^{+0.06}_{-0.05}$
North East	17–36	2T	$0.50^{+0.21}_{-0.18}$	$0.66^{+0.52}_{-0.41}$	$0.57^{+0.21}_{-0.15}$	$0.44^{+0.13}_{-0.09}$	$0.50^{+0.15}_{-0.14}$	$0.64^{+0.15}_{-0.09}$
Far North	20–42	1T	$0.16^{+0.17}_{-0.15}$	$0.00^{+0.20}_{-0.00}$	$0.26^{+0.11}_{-0.10}$	$0.24^{+0.08}_{-0.07}$	$0.36^{+0.13}_{-0.13}$	$0.42^{+0.05}_{-0.04}$
Far North	20–42	2T	$0.25^{+0.26}_{-0.18}$	$0.46^{+0.60}_{-0.46}$	$0.47^{+0.25}_{-0.17}$	$0.35^{+0.15}_{-0.10}$	$0.45^{+0.17}_{-0.16}$	$0.61^{+0.15}_{-0.11}$

\* F-test probability for adding second temperature component

the northeastern regions. We also derived a hardness ratio map of 1.0–1.2 keV to 0.7–1.0 keV observed with XMM (Figure 5). The map shows similar ICM temperatures. The southwest and northwest regions tend to have higher ICM temperatures than the northeast regions.

#### 4.2. Fe abundance distribution of the ICM

The radial profiles of the Fe abundances observed with Suzaku and the pie regions of XMM derived from the 1T model fits are summarized in Figure 6. The values derived from the XMM and Suzaku data are mostly consistent with each other, although the error bars for Suzaku are smaller than those for XMM.

In the Suzaku data, at  $0.03\text{--}0.2\ r_{180}$ , the Fe abundances of the North, North West, and North East fields derived from the 1T model for the ICM are about 0.5–0.6 solar, which is higher than the 0.3–0.4 solar value of the South field. The 2T model for the ICM gives Fe abundances that are systematically higher by  $\sim 20\text{--}50\%$  than the 1T model (Figure 7). Although the errors became larger with the

2T model fits, the Fe abundances of the North and North West fields still tend to be higher than that of the South field (Figure 7).

With the 1T model fits of the XMM-Newton data, the Fe abundances of the ICM were derived out to  $0.3\ r_{180}$ . As derived from the Suzaku observations, at  $0.05\text{--}0.2\ r_{180}$ , the northern regions have higher Fe abundances of 0.5–0.6 solar, whereas the south and west regions have lower values of 0.3–0.4 solar. Beyond  $0.2\ r_{180}$ , the Fe abundance with the 1T model decreases to  $\sim 0.2\text{--}0.3$  solar. The left panel of Figure 8 shows the Fe abundance map derived from the XMM data of the square regions, and the right panel of Figure 8 shows these abundances plotted against the radius from NGC 1399. Within the four central square regions, the Fe abundances are derived from the 2T model fit for the ICM. The southwestern region at  $\sim 0.1\ r_{180}$  has a lower Fe abundance than the other regions at the same radius from NGC 1399.



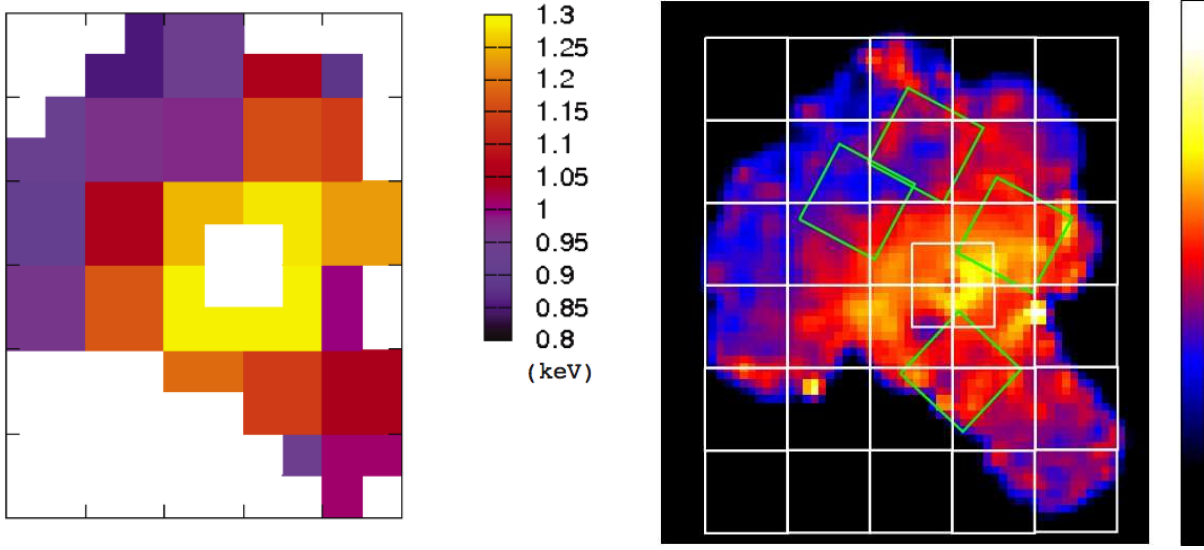


**Fig. 5.** (left) Temperature map of the ICM derived from spectral fitting of the XMM data of the square regions of  $0.1r_{180} \times 0.1r_{180}$  ( $17.5' \times 17.5'$ ). Temperatures of the four small square regions of  $0.05r_{180} \times 0.05r_{180}$  surrounding NGC 1399 are not plotted, because the 2T model is required to fit the spectra. (right) Hardness ratio map of 1.0–1.2 keV to 0.7–1.0 keV. White squares indicate the regions for the spectral analysis in the left panel. Green squares show the four offset regions (South, North West, North East, Far North) observed with Suzaku.

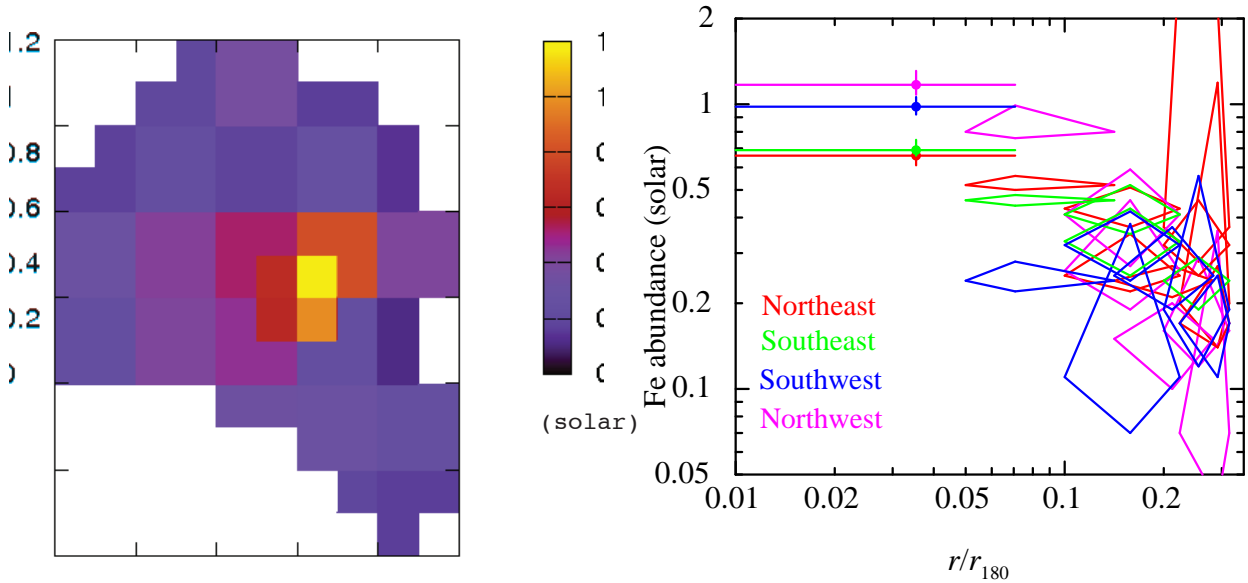


**Fig. 8.** (left) Fe abundance map of the ICM derived from the spectral fitting of the XMM data of the square regions by the 2T model fits for the four central small square regions of  $0.05r_{180} \times 0.05r_{180}$ , and by the 1T model fits for the other regions of  $0.1r_{180} \times 0.1r_{180}$ . NGC 1399 is located at the center of the four small square regions. (right) Radial profile of the ICM of the square regions in the left panel derived from the 2T model (filled circles with solid error bars) and 1T model (diamonds). Red, green, blue and magenta colors correspond to the square regions of northeast, southeast, southwest, and northwest, respectively, of NGC 1399.



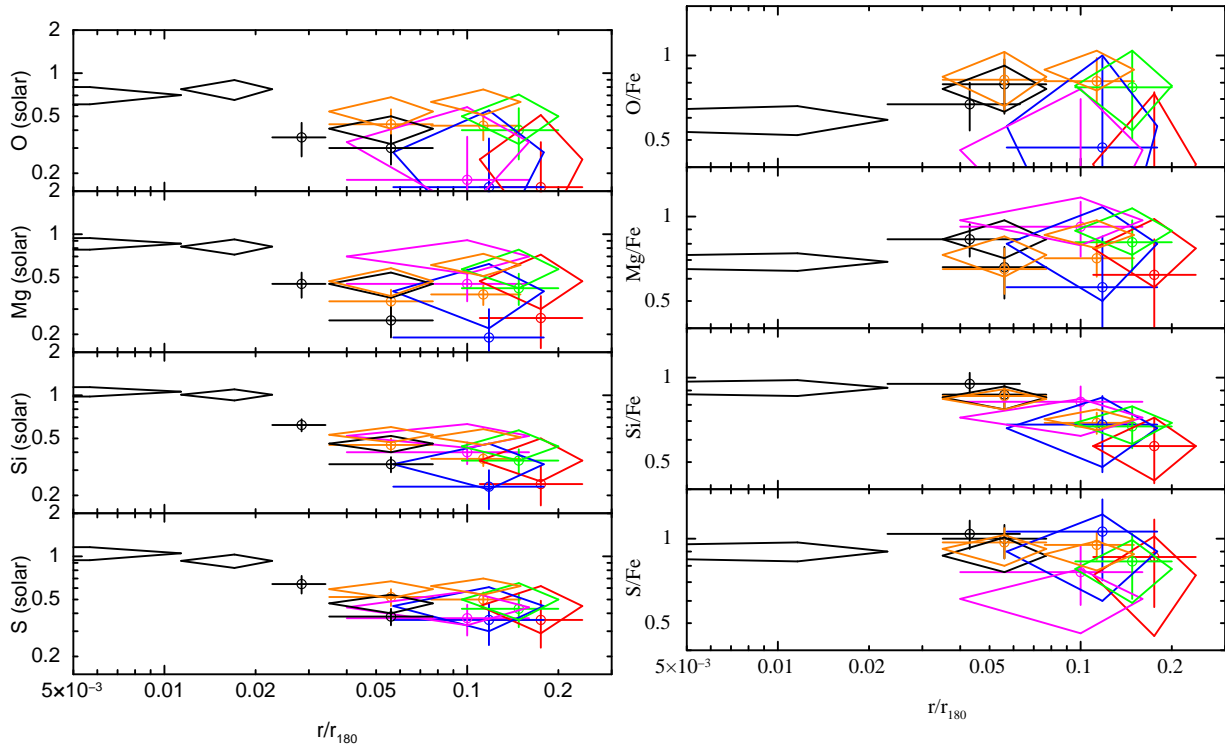


**Fig. 9.** (left) Abundance profiles of O, Mg, Si, and S in the Center (black), North (orange), North West (magenta), South (blue), North East (green), and Far North (red) fields derived from the 1T (open circles) or 2T (diamonds) model for the ICM. Central three radial bins are derived by Matsushita et al. (2007a). (right) Radial profiles of the O/Fe, Mg/Fe, Si/Fe, and S/Fe ratios in solar units. The data within  $0.02 r_{180}$  are weighted averages of the values of the two innermost radial bins.

#### 4.3. Abundances of O, Mg, Si and S

Using the Suzaku observations, we also derived the abundances of O, Ne, Mg, Si, and S (Table 3, Figure 9). From  $0.05 r_{180}$  to  $0.2 r_{180}$ , the Mg, Si, and S abundances derived from the 1T model fits are 0.2–0.5 solar, and 0.3–0.6 solar from the 2T model fits. From the 1T model fits, the abundances of O are 0.2–0.4 solar, with fairly large error bars, and the 2T model yields O abundance values that are larger by 0.1 solar. When the 1T model is used, the derived Ne abundance values tend to be lower than those of other elements, whereas with the 2T model, the Ne abundances are also close to those of Fe.

Right panel of Figure 9 summarizes the abundance ratios of  $\alpha$ -elements divided by the Fe value in solar units. Because the abundances of  $\alpha$ -elements and Fe are correlated, the errors of the abundance ratios were estimated from confidence contours of each  $\alpha$ -element against Fe. The 1T and 2T model fits give similar values for the O/Fe, Mg/Fe, Si/Fe, and S/Fe ratios. The derived abundance ratios are mostly consistent with the absence of radial gradients and azimuthal dependence, although the Si/Fe ratio shows a small negative radial gradient. The weighted averages of the abundance ratios are calculated for the data with similar radial ranges and are summarized in Table 4. The abundance ratios are mostly consistent with the absence of radial dependence. When the values beyond  $6'$  from the 1T model fits are averaged, the abundance ratios of O/Fe, Mg/Fe, Si/Fe, and S/Fe are about

0.7, 0.7, 0.8, and 0.9 in solar units, respectively. The 2T model yields similar abundance ratios within 10–15%.

The weighted averages of Ne/Fe ratios from the 1T and 2T model fits differs by a factor of 3–4. This is because the K-shell lines of Ne are completely mixed with the Fe-L lines, and the Fe-L lines between the 1T and 2T models are different, which may cause a discrepancy. Therefore, the derived abundances of Ne might include fairly large systematic uncertainties.

#### 4.4. Surface brightness and gas density profiles

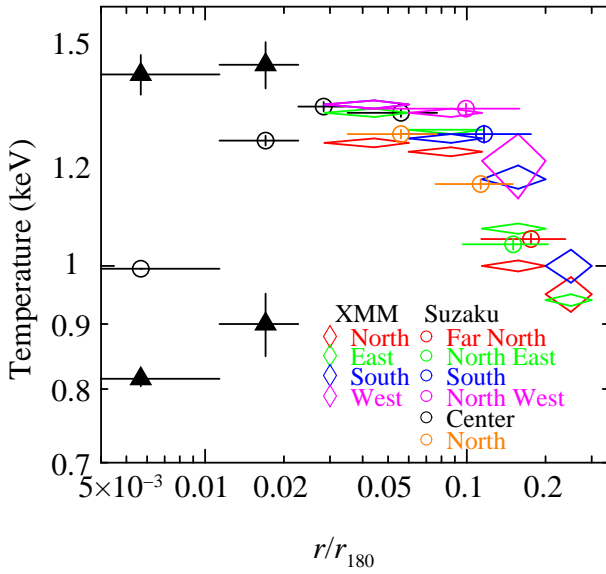
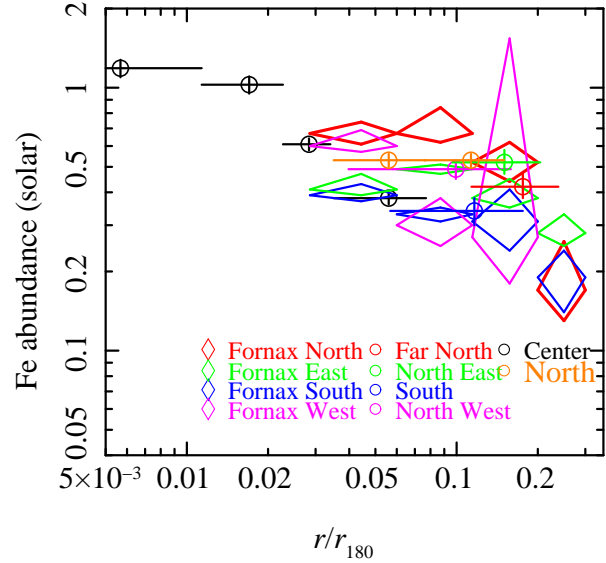
We derived radial profiles of the X-ray surface brightness (left panel of Figure 10) by azimuthally averaging the background-subtracted intensity in the 0.8–1.2 keV energy band of MOS centered on NGC 1399, and on the cluster center derived by Paolillo et al. (2002), which is  $\sim 6'$  northeast of NGC 1399. Here, luminous point sources and a region around NGC 1404 were excluded. For the profile centered on the cluster center, a region around NGC 1399 was also excluded. Beyond  $10'$ , the two radial profiles resemble each other, whereas within  $10'$ , a sharp brightness peak centered on NGC 1399 appears. Similar to Paolillo et al. (2002), we fitted the radial profile centered on NGC 1399 with a sum of three  $\beta$ -models that are all centered on NGC 1399. As shown in Figure 10, the radial profile was roughly reproduced with these three  $\beta$ -models. Considering the similarity of the brightness profiles centered on NGC 1399 and on the cluster center beyond  $10'$ , the density profile of the ICM from the cluster center

**Table 4.** Weighted averages of the abundance ratios in solar units derived from the Suzaku observations

region	model	O/Fe	Ne/Fe	Mg/Fe	Si/Fe	S/Fe
0'-4'*	2T	0.59 <sup>+0.07</sup> <sub>-0.07</sub>	—	0.69 <sup>+0.05</sup> <sub>-0.05</sub>	0.92 <sup>+0.06</sup> <sub>-0.06</sub>	0.90 <sup>+0.07</sup> <sub>-0.07</sub>
6'-42'†	1T	0.74 <sup>+0.09</sup> <sub>-0.09</sub>	0.34 <sup>+0.16</sup> <sub>-0.17</sub>	0.70 <sup>+0.06</sup> <sub>-0.05</sub>	0.77 <sup>+0.03</sup> <sub>-0.03</sub>	0.94 <sup>+0.06</sup> <sub>-0.06</sub>
6'-42'†	2T	0.76 <sup>+0.08</sup> <sub>-0.08</sub>	1.23 <sup>+0.20</sup> <sub>-0.21</sub>	0.83 <sup>+0.06</sup> <sub>-0.06</sub>	0.75 <sup>+0.04</sup> <sub>-0.03</sub>	0.84 <sup>+0.06</sup> <sub>-0.06</sub>
6'-13'†	1T	0.80 <sup>+0.13</sup> <sub>-0.13</sub>	0.42 <sup>+0.27</sup> <sub>-0.27</sub>	0.66 <sup>+0.08</sup> <sub>-0.09</sub>	0.87 <sup>+0.05</sup> <sub>-0.06</sub>	0.99 <sup>+0.08</sup> <sub>-0.08</sub>
6'-13'†	2T	0.79 <sup>+0.12</sup> <sub>-0.11</sub>	1.31 <sup>+0.30</sup> <sub>-0.30</sub>	0.77 <sup>+0.09</sup> <sub>-0.09</sub>	0.84 <sup>+0.05</sup> <sub>-0.05</sub>	0.90 <sup>+0.09</sup> <sub>-0.08</sub>
7'-31'†	1T	0.70 <sup>+0.14</sup> <sub>-0.13</sub>	0.32 <sup>+0.27</sup> <sub>-0.25</sub>	0.74 <sup>+0.09</sup> <sub>-0.09</sub>	0.72 <sup>+0.05</sup> <sub>-0.06</sub>	0.91 <sup>+0.09</sup> <sub>-0.09</sub>
7'-31'†	2T	0.78 <sup>+0.13</sup> <sub>-0.13</sub>	1.28 <sup>+0.33</sup> <sub>-0.33</sub>	0.88 <sup>+0.09</sup> <sub>-0.09</sub>	0.71 <sup>+0.05</sup> <sub>-0.05</sub>	0.82 <sup>+0.08</sup> <sub>-0.10</sub>
17'-42'†	1T	0.63 <sup>+0.22</sup> <sub>-0.22</sub>	0.20 <sup>+0.37</sup> <sub>-0.20</sub>	0.74 <sup>+0.13</sup> <sub>-0.13</sub>	0.64 <sup>+0.11</sup> <sub>-0.11</sub>	0.83 <sup>+0.21</sup> <sub>-0.22</sub>
17'-42'†	2T	0.63 <sup>+0.20</sup> <sub>-0.18</sub>	0.75 <sup>+0.75</sup> <sub>-0.75</sub>	0.84 <sup>+0.14</sup> <sub>-0.13</sub>	0.65 <sup>+0.08</sup> <sub>-0.08</sub>	0.77 <sup>+0.17</sup> <sub>-0.16</sub>

\* weight average within 4' from NGC 1399 from Matsushita et al. (2007a)

† Weighted averages of abundance ratios at 6'-42', 6'-13' (Center and North), 7'-31' (South and North West), and 17'-42' (North East and Far North)

**Fig. 4.** The ICM temperatures from Suzaku data versus radius of NGC 1399 in units of  $r_{180}$  for the Center (black open circles), North (orange open circles), Far north (red open circle), North East (green open circle), South (blue open circle), and North West (magenta open circle) fields derived from the 1T model fit for the ICM, and those from the 2T (black filled triangles) model fits within the central two radial bins. The data of the innermost three radial bins are from Matsushita et al. (2007a). The ICM temperatures of the pie regions of XMM with the 1T model fits are plotted as diamonds. Red, green, blue and magenta correspond to the northern, eastern, southern and western pie regions, respectively.**Fig. 6.** Radial profile of the Fe abundance of the ICM derived from the 1T model fits for the ICM using Suzaku data (open circles) and XMM data of the pie regions (diamonds). Colors have the same meanings as in Figure 4. Data of the innermost three radial bins are from Matsushita et al. (2007a). Here, those of the innermost two radial bins are derived from the 2T model fits. Region at 0.035–0.07  $r_{180}$  of the Center field covers mostly the south of NGC 1399.

should also be similar to that from NGC 1399.

To study the azimuthal variation in the radial brightness profile, we divided the images centered on NGC 1399, into four sectors—north, west, south, and east—and derived radial brightness profiles within each sector. The radial profiles of the four sectors are plotted in the middle panel of Figure 10. At  $\sim 20'$  ( $\sim 0.1r_{180}$ ), the brightness levels in the north and east sectors are higher by a factor of 2–3 than those in the south and west sectors. We also derived radial brightness profiles in the four sectors centered on the cluster center. The discrepancy in the brightness levels of the four sectors became smaller (right panel of Figure 10).

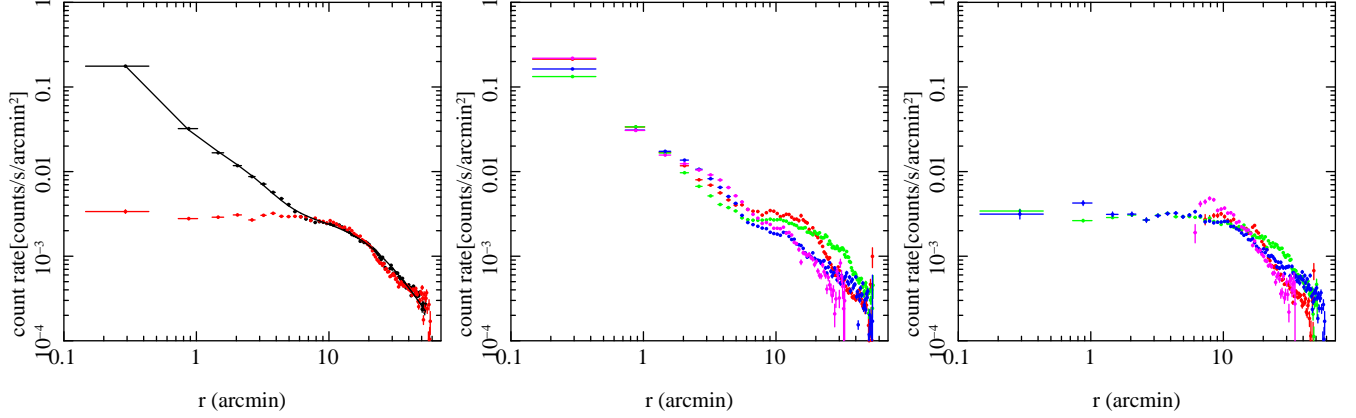


**Fig. 10.** (Left) Radial profiles of the surface brightness centered on NGC 1399 (black) and on the cluster center (red) by Paolillo et al. (2002), which is  $\sim 6'$  northeast of NGC 1399. The solid line represents the best-fit triple  $\beta$ -model. (middle) Radial profiles of north (red), west (magenta), east (green), and south (blue) sectors centered on NGC 1399. (right) The same as the middle panel, but centered on the cluster center.

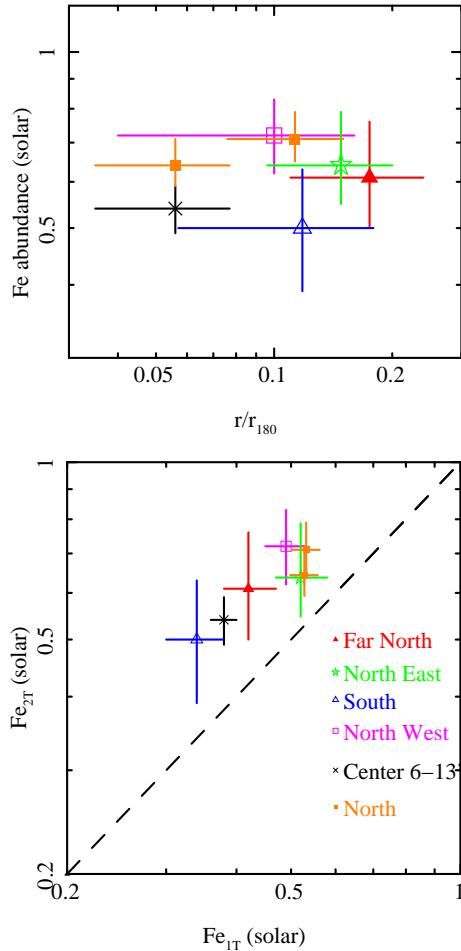


**Fig. 7.** (upper panel) Fe abundance of the ICM observed with Suzaku derived from the 2T model fits plotted against those from the 1T model fits. Black cross, orange filled squares, blue open triangle, magenta open square, green star, and red filled triangle correspond to the Center, North, South, Northwest, Northeast, and Far North fields, respectively. (lower panel) Radial profiles of the Fe abundance of the ICM derived from the 2T model fits of the Suzaku data.

## 5. Discussion

### 5.1. Comparison of the Fe abundance profiles with those of other systems

In Figure 11, the radial profiles of the Fe abundance in the Fornax cluster derived from the 1T and 2T model fits are compared with those in other groups of galaxies observed with Suzaku: the NGC 507 group (Sato et al. 2009a), HGC 62 group (Tokoi et al. 2008), the NGC 5044 group (Komiya et al. 2009), and the fossil group NGC 1550 (Sato et al. 2010). Here, the Fe abundances of the Fornax cluster at similar radial ranges from NGC 1399 are averaged. Considering the possible uncertainties in the Fe-L atomic data and background components, we cannot conclude that the 2T model fit is better than that the 1T model, because the two models yield similar  $\chi^2$  values in the region with low surface brightness.

The Fe abundance within  $0.03 r_{180}$  from NGC 1399 is about 1 solar. At  $0.05 r_{180}$  of the Fornax cluster, the 1T and 2T model fits give the Fe abundances of  $\sim 0.4$  and  $\sim 0.5$  solar, respectively. These values are significantly smaller than the Fe abundances of NGC 5044 and NGC 507 groups, at  $\sim 0.05 r_{180}$  which are derived from the 2T model fits. At  $0.1$ – $0.2 r_{180}$ , the Fe abundances of the Fornax cluster are 0.4 solar and 0.6 solar, from the 1T and 2T model fits, respectively. The value from the 2T model fits is close to those of the NGC 507 and NGC 5044 groups, although HGC 62, a compact group of galaxies, and NGC 1550, a fossil group, tend to have smaller Fe abundances when the 2T model fits are used. These values are also similar to those of the clusters of galaxies (Leccardi & Molendi 2008; Matsushita 2011). There is no systematic difference between the poor systems and the clusters of galaxies regarding the Fe abundance of the ICM at  $0.1$ – $0.2 r_{180}$ .

In Figure 11, the Fe abundances derived from the Suzaku data are compared with those of the best-fit regression relations from Chandra data (Rasmussen & Ponman 2007) and from XMM data (Johnson et al. 2011).

Here, we rescaled for the differences in the definition of the solar abundance table and virial radius. Johnson et al. (2011) showed that within  $\sim 0.3 r_{180}$ , the 2T fit gives abundances that are higher by a factor of  $\sim 1.5$  than those of the 1T fit. Using the same temperature modeling of the ICM, the Suzaku results agree very well with the regression relations from XMM data (Johnson et al. 2011). In contrast, the results of Suzaku and XMM using the 2T model are systematically higher than the best-fit regression line of the groups derived with the Chandra data (Rasmussen & Ponman 2007; Rasmussen & Ponman 2009), where 2T model results are adopted when the 2T model gave different abundances from the 1T model. The Fe abundances by Rasmussen & Ponman (2007) show a significant scatter at given radius in units of  $r_{500}$  and some groups have comparable abundance profiles with those observed with Suzaku. The radial profile of Fe abundance of the HCG 62 system with Suzaku is consistent with those of the Chandra groups. Therefore, a major part of the differences in the Fe abundance should be caused by the differences in the sample. Different assumptions regarding the abundance ratio, i.e. VAPEC, or APEC, may not be responsible for the discrepancy, since the abundance patterns of these groups of galaxies derived with Suzaku do not differ greatly from the solar ratio. On the other hand, as shown in Komiyama et al. (2009), in regions with low surface brightness, uncertainties in the Galactic emission can also affect the derived Fe abundance.

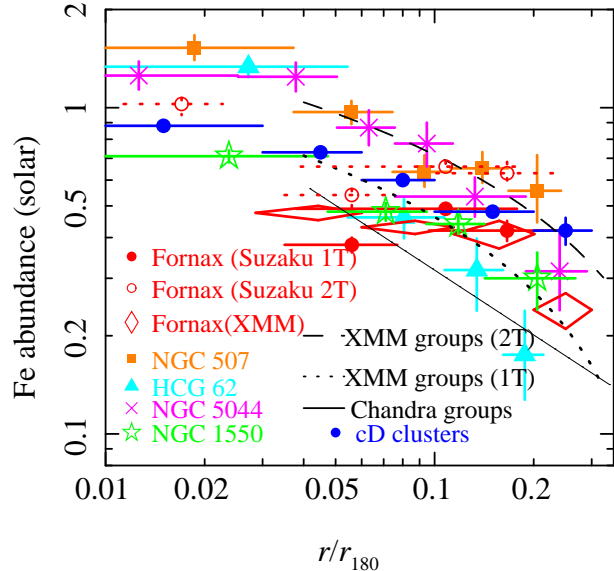
### 5.2. ICM abundance pattern and contributions from SN Ia and SN II

Figure 12 summarizes the radial profiles of the O/Fe, Mg/Fe, Si/Fe, and S/Fe ratios in five poor systems (the Fornax cluster, the NGC 5044 group, the HCG 62 group, and the NGC 507 group, and a fossil group, NGC 1550), and clusters of galaxies, A262 ( $kT \sim 2\text{keV}$ ), and AWM 7 ( $kT \sim 4\text{keV}$ ). The radial profiles of the Fornax cluster were the weighted averages of similar radial ranges derived from the Suzaku data summarized in Table 4. In particular, outside the cool cores at  $0.05\text{--}0.2 r_{180}$ , the scatter in the abundance ratios, except for the Mg/Fe ratios, among these systems is relatively small. The scatter in the Mg/Fe ratios may be due to the systematic uncertainties in the Fe-L lines around the Mg-K lines.

In these poor systems, the abundance ratios exhibit no significant radial dependence. The abundance pattern of O/Mg/Si/S/Fe in the offset regions of the Fornax cluster is similar to those of the other groups of galaxies. Out to  $0.3 r_{180}$  there is no hint of increase in the ratio of  $\alpha$ -elements to Fe abundances in these poor systems. These results indicate that both SN Ia and SN II products have been mixed into the ICM, and that the ratio of the two types of SN in the Fornax cluster is similar to those of the other groups of clusters of galaxies.

### 5.3. Radial profiles of the metal-mass-to-light ratios

Because most of metals in the ICM synthesized in galaxies, the metal-mass-to-light ratio is a useful measure for studying the chemical evolution of clusters of galaxies.



**Fig. 11.** Radial profiles of the Fe abundance in the Fornax cluster observed with Suzaku derived from the 1T model (red filled circles with solid lines) and the 2T model (red open circles with dotted lines) and with XMM from the 1T model (red diamonds). Here, the Fe abundances with similar radial ranges are averaged. Those of the NGC 507 group (orange filled squares; Sato et al. 2009a), HCG 62 group (cyan filled triangles; Tokoi et al. 2008), NGC 5044 group (magenta crosses; Komiyama et al. 2009), and a fossil group, NGC 1550 (green stars; Sato et al. 2010). The weighted average of relaxed clusters with a cD galaxy at their center observed with XMM (blue filled circles; Matsushita 2011) and the best-fit regression relations for groups of galaxies observed with Chandra (black solid line: Rasmussen & Ponman 2007) and cool-core groups observed with XMM (2T: black dashed line, 1T: black dotted line; Johnson et al. 2011) are also plotted.

To estimate the metal mass, we used the radial brightness profile derived in section 4.4, and derived the gas density and gas mass profiles. Then, integrated mass profiles of O and Fe were derived from the gas mass and abundance profiles using the 1T model fits. The 2T model fits yielded 10–20% smaller normalizations of the ICM and several tens of % higher Fe abundances in the Fornax cluster compared with the 1T model fits. Therefore, the total metal mass may have systematic uncertainties of several tens of percent, due to uncertainties in the temperature structure.

Because the K-band luminosity of a galaxy correlates well with the stellar mass, we calculated the luminosity profile of the K-band. We collected K-band magnitudes of galaxies in  $6 \times 6 \text{ deg}^2$  box centered on NGC 1399 from the Two Micron All Sky Survey (2MASS). NGC 1399 has an apparent magnitude of  $m_K = 6.440$ , or  $\log L_K/L_{K,\odot} = 11.4$  using the foreground Galactic extinction  $A_K = 0.005$  (Schlegel et al. 1998) from the NASA/IPAC Extragalactic Database. The average surface brightness in the region at  $150' < r < 176'$  ( $0.86r_{180} < r < 1.0r_{180}$ ) is subtracted as the background. Within  $0.3 r_{180}$  of the Fornax cluster,  $\sim 10$  early-type galaxies dominate the K-band luminosity.



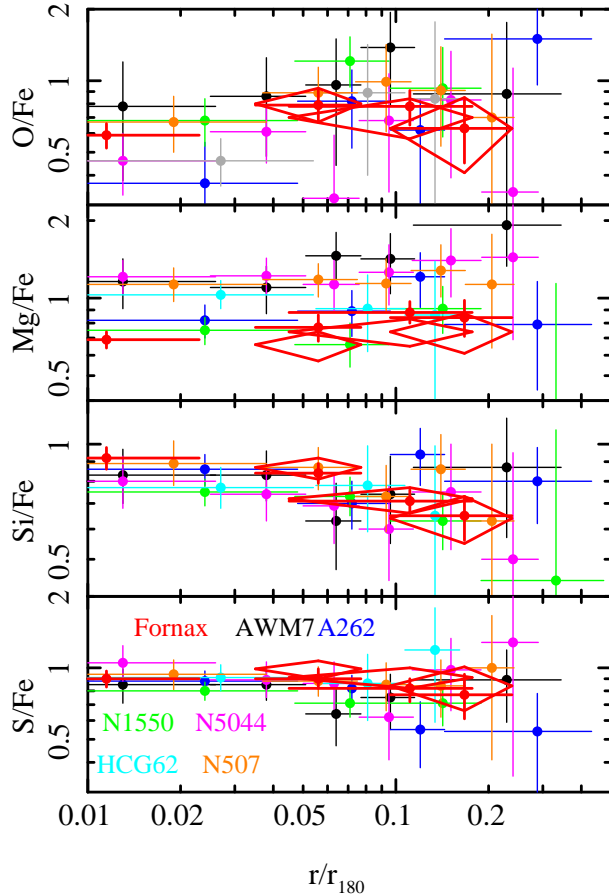


**Fig. 12.** Radial profiles of O/Fe, Mg/Fe, Si/Fe, and S/Fe ratios of the Fornax cluster (red) from the 1T (diamonds) and 2T (filled circles) model fits. Here, these values are weighted averages of similar radial ranges. Radial profiles of the fossil group NGC 1550 (green; Sato et al. 2010), the NGC 5044 group (magenta; Komiyama et al. 2009), HCG 62 (light blue; Tokoi et al. 2008), and the NGC 507 group (orange; Sato et al. 2009a), and those of the clusters of galaxies, AWM 7 (black; Sato et al. 2008), and A262 (blue; Sato et al. 2009b).

NGC 1399 dominates the luminosity in the region  $r < \sim 0.04 r_{180}$ . At  $r \sim 0.06 r_{180}$ , NGC 1404, a bright galaxy, causes a break in the luminosity profiles. At  $\sim 0.2 r_{180}$ , several early-type galaxies including NGC 1380 contribute to the luminosity profiles.

The integrated mass-to-light ratios for O and Fe (OMLRs and IMLRs) using the K-band luminosities are summarized in Figure 13. The error bars of the mass-to-light ratios include only abundance errors. The OMLR and IMLR profiles are not smooth because of several luminous galaxies in the Fornax cluster. The profiles increase with radius out to  $0.2 r_{180}$ . However, the IMLR profile became flat from  $0.2 r_{180}$  to  $0.3 r_{180}$ , due to increase of K-band luminosity from several luminous early-type galaxies. We extrapolated the best-fit three  $\beta$ -model of the surface brightness of the ICM, assuming that Fe abundance of the ICM beyond  $0.3 r_{180}$  is the same as in that of the best-fit value at  $0.2\text{--}0.3 r_{180}$ . Then, at  $0.5 r_{180}$ , the

IMLR may not increase very much (Figure 13).

Figure 13 compares the derived OMLRs and IMLRs of the Fornax cluster with those of the NGC 5044 group (Komiyama et al. 2009), the fossil group NGC 1550 (Sato et al. 2010), and the Abell 262 cluster ( $kT \sim 2$  keV; Sato et al. 2009b), and IMLR of the AWM 7 cluster ( $kT \sim 4$  keV; Sato et al. 2008). In contrast to the Fornax cluster, central galaxies dominates the K-band luminosity in the NGC 5044 group, the fossil group NGC 1550, and Abell 262, and most of the other galaxies are dwarfs. Therefore, the profiles of these systems are smoother than those of the Fornax cluster. Within  $0.1 r_{180}$ , the IMLR and OMLR of the Fornax cluster are much smaller than those of the other systems. The similar IMLR profiles of the other systems within  $0.1 r_{180}$  indicate that the recent metal supplies from the central galaxies are typical. The small IMLR in the Fornax cluster indicates that the accumulation time scale of metals from the cD galaxy should be shorter, reflecting the fact that the cD galaxy is not located at the cluster center and moving. At  $0.1\text{--}0.3 r_{180}$ , the IMLR of the Fornax cluster is still an order of magnitude smaller than those of the rich systems, AWM 7, Abell 262, and NGC 1550. The IMLR of these three systems increase with radius in the same way from  $0.1 r_{180}$  to  $0.3\text{--}0.5 r_{180}$ . However, the IMLRs of the NGC 5044 group is constant from  $0.1 r_{180}$  to  $0.3 r_{180}$ , and at  $0.3 r_{180}$ , the IMLR of the NGC 5044 group is nearly an order of magnitude larger than that of the Fornax cluster. The extrapolated value of the IMLR at  $0.5 r_{180}$  of the Fornax cluster are still over an order of magnitude smaller than those of the NGC 1550 group and Abell 262 cluster.

Rasmussen & Ponman (2009) found that the IMLR derived from Chandra and Suzaku are consistent with each other, despite the systematic difference in the derived Fe abundance. This is because a larger Fe abundance is associated with a smaller gas mass in lower temperature groups.

#### 5.4. Dynamical history of the Fornax cluster

Chandra observations revealed that NGC 1399 is moving within the Fornax cluster (Scharf et al. 2005). The X-ray emission of the northeast region of the Fornax cluster is brighter than that of the south region. The ICM temperature of the southwest region is higher than that of the northeast region. The lower ICM temperature and the higher brightness of the northeast region indicate lower entropy in the ICM. The Fe abundance of the northeast region at  $0.1\text{--}0.2 r_{180}$  is higher than that of the southwest region at the same radius. Lower entropy and the higher Fe abundance are usually observed in the cool cores. Therefore, the cD galaxy may have traveled from the center of the cluster to the south due to recent dynamical evolution, as suggested by the optical dynamical observations by Dunn & Jerjen (2006).

Recent dynamical evolution might have hindered the strong concentration of hot gas in the central region of the Fornax cluster. The X-ray luminosity within  $4r_e$  of NGC 1399 is smaller by a factor of 20 than that of NGC 5044 (Matsushita 2001; Nagino & Matsushita 2009). The

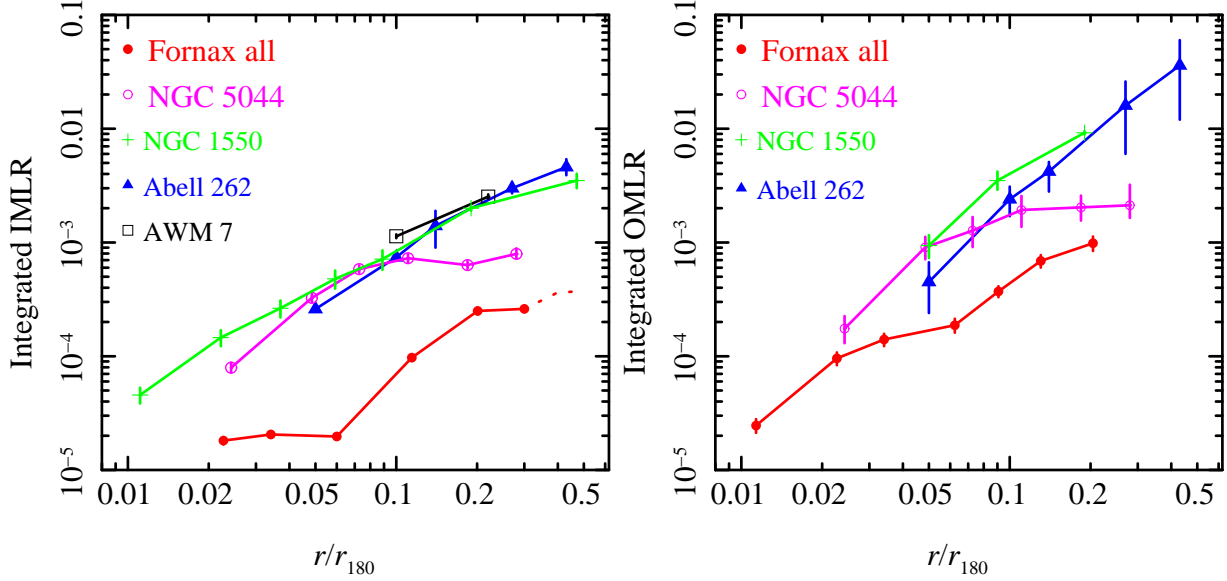


**Fig. 13.** Radial profiles of integrated IMLR (left panel) and OMLR (right panel) in the K-band of the Fornax cluster (red filled circles), NGC 5044 group (purple open circle; Komiyama et al. 2009), NGC 1550 group (green crosses; Sato et al. 2010), Abell 262 cluster (blue filled triangles; Sato et al. 2009b), and AWM 7 cluster (black open squares; Sato et al. 2008). Dotted line for the Fornax cluster represent extrapolated values using the surface brightness and the Fe abundances within  $0.3 r_{180}$

X-ray luminosity of NGC 1550 is also higher by an order of magnitude than that of NGC 1399 (Fukazawa et al. 2006). For NGC 1399, the central Fe peak is narrower and the IMLR is much smaller than those of the other groups. Some merging clusters also have smaller scale of Fe peaks (Matsushita 2011). During cluster merging, mixing of the ICM could destroy the central Fe peak. The Fornax cluster is also in a stage of dynamical evolution, and may be in a phase of central Fe peak destruction. Then, recent supply of metals from NGC 1399 via stellar mass loss and SN Ia produces a smaller Fe abundance peak than in the other groups.

##### 5.5. Metal enrichment and feedback in the groups and clusters

The metal distribution in the ICM can be a powerful tracer of the history of gas heating in the early epoch, because the relative timing of metal enrichment and heating should affect the present amount and distribution of the metals in the ICM. The observed IMLRs in poor systems are scattered by an order of magnitude, whereas, the Fe abundance profiles are similar among these systems and also similar to those of clusters. The Fornax cluster has the smallest IMLR out to  $0.3 r_{180}$ . If all galaxies synthesize a similar amount of metals per unit stellar mass, the observed low IMLR and similar Fe abundance compared with other systems indicate that a significant fraction of the Fe was synthesized in an early phase of cluster evolution. If metal enrichment occurred before energy injection, the poor systems would carry relatively smaller metal mass with a smaller gas mass than rich clusters, whereas, the metal abundance would be quite similar to those in rich clusters. Dynamical evolutions may also

change the gas distribution, but not the abundance of the gas. In contrast, if metal enrichment occurred after energy injection, the metal mass becomes comparable to those in rich clusters and indicates a higher abundance reflecting a lower gas mass.

Similar to rich clusters, most of the stellar light in the Fornax cluster originates from bright old early-type galaxies (Kuntschner 2000). The stellar metallicity and [Mg/Fe] ratios of the central regions of these galaxies are similar to those of similar size in rich clusters (Kuntschner 2000). The O/Mg/Fe abundance pattern of the hot interstellar medium (ISM) of NGC 1399 and NGC 1404 in the Fornax cluster derived from the Suzaku observations (Matsushita et al. 2007a) are similar to those of NGC 4636 (Hayashi et al. 2009) in the Virgo cluster. Reflection grating spectrometer (RGS) observations onboard the XMM showed that the O/Fe ratio of the ISM in NGC 1404 in the Fornax cluster is similar to those of elliptical galaxies in the Virgo cluster (Werner et al. 2009). Because the hot ISM in elliptical galaxies results from the accumulation of stellar mass loss and the ejecta from recent SNe Ia, the observed similarity of the abundance patterns of the hot ISM suggests that the stellar metallicity and SN Ia rate do not differ greatly between the present elliptical galaxies in the Fornax and Virgo clusters. These results indicate that stars in elliptical galaxies in the Fornax cluster were enriched in the same way as those in rich clusters.

The observed higher stellar mass fraction and the lower gas mass fraction within  $r_{500}$  in poor systems, are sometimes interpreted as demonstrating that the star formation efficiency depends on the system mass. However, the similarity in abundances in the ICM between groups and clusters and a scatter in the metal-mass-to-light ratios can

be better explained by early metal enrichment, as discussed in Matsushita (2011), on the basis of the relatively flat abundance profiles of Fe in the ICM in clusters of galaxies.

## 6. Summary and Conclusion

Suzaku and the XMM observed the Fornax cluster out to  $0.2\text{--}0.3\ r_{180}$ , and derived the temperature and O, Mg, Si, S, and Fe abundances in the ICM quite accurately. The ICM temperature decreases from 1.5 keV near the cD galaxy NGC 1399 to 1 keV in the outer region. The Fe abundance around NGC 1399 is about one solar, and the central Fe abundance peak is narrower than that in the groups and clusters with cool cores. The Fe abundance drops to  $0.3\text{--}0.5$  solar at  $0.1\text{--}0.2\ r_{180}$ , which is similar to the values in other groups and clusters. The abundance ratios, O/Fe, Mg/Fe, Si/Fe, and S/Fe, are close to the solar ratio, similar to other groups and clusters of galaxies. The abundance pattern indicates that both SN Ia and SN II products have been mixed into the ICM, and the ratio of the two types of SN in the Fornax cluster is similar to those of other groups and clusters of galaxies.

The northeast region of NGC 1399 has a lower ICM temperature, higher abundances and higher surface brightness than the southwest regions. Therefore, the cD galaxy may have traveled from the center of the cluster to the south owing to recent dynamical evolution.

Out to  $0.3\ r_{180}$ , the IMLR of the Fornax cluster is an order of magnitude smaller than that of other groups and clusters. The metal distribution in the ICM can be used as a tracer of the past history of heating and enrichment in clusters of galaxies. Scatter in the IMLR and similarity in the abundances in the ICM indicate early metal synthesis in groups and clusters.

## References

- Anders, E., & Grevesse, N. 1989, *Geochim. Cosmochim. Acta*, 53, 197
- Arnaud, M., Pointecouteau, E., & Pratt, G. W. 2007, *A&A*, 474, L37
- Borgani, S., Finoguenov, A., Kay, S. T., Ponman, T. J., Springel, V., Tozzi, P., & Voit, G. M. 2005, *MNRAS*, 361, 233
- Buote, D. A. 2002, *ApJ*, 574, L135
- Dickey, J. M., & Lockman, F. J. 1990, *ARA&A*, 28, 215
- Dunn, L. P., & Jerjen, H. 2006, *AJ*, 132, 1384
- Evrard, A. E., Metzler, C. A., & Navarro, J. F. 1996, *ApJ*, 469, 494
- Finoguenov, A., Ponman, T. J., Osmond, J. P. F., & Zimer, M. 2007, *MNRAS*, 374, 737
- Fukazawa, Y., Botoya-Nones, J. G., Pu, J., Ohto, A., & Kawano, N. 2006, *ApJ*, 636, 698
- Giodini, S., et al. 2009, *ApJ*, 703, 982
- Hayashi, K., Fukazawa, Y., Tozuka, M., Nishino, S., Matsushita, K., Takei, Y., & Arnaud, K. A. 2009, *PASJ*, 61, 1185
- Ishisaki, Y., et al. 2007, *PASJ*, 59, 113
- Johnson, R., Ponman, T. J., & Finoguenov, A. 2009, *MNRAS*, 395, 1287
- Johnson, R., Finoguenov, A., Ponman, T. J., Rasmussen, J., & Sanderson, A. J. R. 2011, *MNRAS*, 413, 2467
- Kaiser, N. 1991, *ApJ*, 383, 104
- Komiyama, M., Sato, K., Nagino, R., Ohashi, T., & Matsushita, K. 2009, *PASJ*, 61, S337
- Koyama, K. et al. 2007, *PASJ*, 59, 23
- Kuntschner, H. 2000, *MNRAS*, 315, 184
- Kuntz, K. D., & Snowden, S. L. 2008, *A&A*, 478, 575
- Leccardi, A., & Molendi, S. 2008, *A&A*, 487, 461
- Lodders, K. et al. 2003, *ApJ*, 591, 1220
- Lumb, D. H., Warwick, R. S., Page, M., & De Luca, A. 2002, *A&A*, 389, 93
- Machacek, M., Dosaj, A., Forman, W., Jones, C., Markevitch, M., Vikhlinin, A., Warmflash, A., & Kraft, R. 2005, *ApJ*, 621, 663
- Makishima, K., et al. 2001, *PASJ*, 53, 401
- Markevitch, M., Forman, W. R., Sarazin, C. L., & Vikhlinin, A. 1998, *ApJ*, 503, 77
- Matsushita, K. 2001, *ApJ*, 547, 693
- Matsushita, K., Finoguenov, A., & Böhringer, H. 2003, *A&A*, 401, 443
- Matsushita, K., et al. 2007a, *PASJ*, 59, 327
- Matsushita, K., Böhringer, H., Takahashi, I., & Ikebe, Y. 2007b, *A&A*, 462, 953
- Matsushita, K. 2011, *A&A*, 527, A134
- Mitsuda, K., et al. 2007, *PASJ*, 59, 1
- Nagino, R., & Matsushita, K. 2009, *A&A*, 501, 157
- Paolillo, M., Fabbiano, G., Peres, G., & Kim, D.-W. 2002, *ApJ*, 565, 883
- Ponman, T. J., Cannon, D. B., & Navarro, J. F. 1999, *Nature*, 397, 135
- Ponman, T. J., Sanderson, A. J. R., & Finoguenov, A. 2003, *MNRAS*, 343, 331
- Pratt, G. W., et al. 2010, *A&A*, 511, A85
- Rasmussen, J., & Ponman, T. J. 2007, *MNRAS*, 380, 1554
- Rasmussen, J., & Ponman, T. J. 2009, *MNRAS*, 399, 239
- Sato, K., et al. 2007, *PASJ*, 59, 299
- Sato, K., Matsushita, K., Ishisaki, Y., Sasaki, S., Ohashi, T., Yamasaki, N. Y., & Ishida, M. 2008, *PASJ*, 60, 333
- Sato, K., Matsushita, K., Ishisaki, Y., Yamasaki, N. Y., Ishida, M., & Ohashi, T. 2009a, *PASJ*, 61, S353
- Sato, K., Matsushita, K., & Gastaldello, F. 2009b, *PASJ*, 61, S365
- Sato, K., Kawaharada, M., Nakazawa, K., Matsushita, K., Ishisaki, Y., Yamasaki, N. Y., & Ohashi, T. 2010, *PASJ*, 62, 1445
- Schlegel, D. J., Finkbeiner, D. P., & Davis, M. 1998, *ApJ*, 500, 525
- Scharf, C. A., Zurek, D. R., & Bureau, M. 2005, *ApJ*, 633, 154
- Simionescu, A., Werner, N., Böhringer, H., Kaastra, J. S., Finoguenov, A., Brüggen, M., & Nulsen, P. E. J. 2009, *A&A*, 493, 409
- Sun, M., Voit, G. M., Donahue, M., Jones, C., Forman, W., & Vikhlinin, A. 2009, *ApJ*, 693, 1142
- Smith, R. K., Brickhouse, N. S., Liedahl, D. A., & Raymond, J. C. 2001, *ApJL*, 556, L91
- Tamura, T., Kaastra, J. S., Makishima, K., & Takahashi, I. 2003, *A&A*, 399, 497
- Tawa, N., et al. 2008, *PASJ*, 60, 11
- Tokoi, K., et al. 2008, *PASJ*, 60, 317



- Vikhlinin, A., Kravtsov, A., Forman, W., Jones, C., Markevitch, M., Murray, S. S., & Van Speybroeck, L. 2006, ApJ, 640, 691
- Voit, G. M., Balogh, M. L., Bower, R. G., Lacey, C. G., & Bryan, G. L. 2003, ApJ, 593, 272
- Werner, N., Zhuravleva, I., Churazov, E., Simionescu, A., Allen, S. W., Forman, W., Jones, C., & Kaastra, J. S. 2009, MNRAS, 398, 23
- Yoshino, T., et al. 2009, PASJ, 61, 805